Real-time estimation of negative electrode potential and state of charge of lithium-ion battery based on a half-cell-level equivalent circuit model

Cheng Zhang, Tazdin Amietszajew, Shen Li, Monica Marinescu, Gregory Offer, Chongming Wang, Yue Guo and Rohit Bhagat

Original citation:
Zhang, C., Amietszajew, T., Li, S., Marinescu, M., Offer, G., Wang, C., Guo, Y. and Bhagat, R., 2022. Real-time estimation of negative electrode potential and state of charge of lithium-ion battery based on a half-cell-level equivalent circuit model. *Journal of Energy Storage*, *51*, 104362.
https://doi.org/10.1016/j.est.2022.104362

DOI 10.1016/j.est.2022.104362
ISSN 2352-152X

Publisher: Elsevier

Journal of Energy Storage 51 (2022) 104362

Contents lists available at ScienceDirect

Journal of Energy Storage

journal homepage: www.elsevier.com/locate/est

Research Papers

Real-time estimation of negative electrode potential and state of charge of lithium-ion battery based on a half-cell-level equivalent circuit model

Cheng Zhang [a,*], Tazdin Amietszajew [a], Shen Li [b], Monica Marinescu [b], Gregory Offer [b], Chongming Wang [a], Yue Guo [a], Rohit Bhagat [a]

[a] Institute for Clean Growth and Future Mobility, Coventry University, CV1 5FB, United Kingdom
[b] Department of Mechanical Engineering, Imperial College London, SW7 2AZ, United Kingdom

ARTICLE INFO

Keywords:
Lithium-ion battery
Half-cell ECM model
Reference electrode
Negative electrode potential
Kalman filter estimation

ABSTRACT

Equivalent circuit models (ECMs) have been widely used for capturing the electrical behaviour of lithium-ion batteries (LIBs). However, one limitation of the conventional full-cell level ECM is that it cannot capture the battery's internal states at half-cell level, e.g., the negative electrode (NE) potential. Real-time monitoring of NE potential is highly desirable for improving battery performance and safety, as it can prevent lithium plating which occurs when the NE potential drops below a threshold value. This paper proposes an easy-to-implement framework for real-time estimation of the NE potential of LIBs. An ECM at half-cell level is developed and parametrised by a bespoke experimental method, exemplified on a commercial 21700 LIB cell. The cell is instrumented with a lithium reference electrode that enables direct measurement of the per-electrode potential. Based on the developed model, an extended Kalman filter is implemented to estimate the battery's NE potential and SoC in real-time using only onboard available signals including the terminal current and voltage. Experimental results show that the proposed method achieves high modelling and estimation accuracy. The root mean square error of the real-time NE potential estimation is below 8 mV. The low computational complexity of the developed algorithm can facilitate practical implementation in commercial BMS.

1. Introduction

Lithium-ion batteries (LIBs) are widely used in electric vehicles and stationary storage systems which play a key role in decarbonizing the transport and energy sectors [1]. A battery management system (BMS) is essential to monitor and control the real-time operation of the battery system to ensure safety and efficiency. To enhance the BMS functionality, a battery model is usually required to predict the system dynamics under various operating conditions [2]. Among different types of models, including electrochemical models, reduced order models and black-box models [3–5], the equivalent circuit model (ECM) is frequently favoured for onboard implementation in BMS for parameter and state estimation [6–8] and control [9,10], due to its low computational cost, ease of parameterisation and desirable accuracy.

One significant limitation of the conventional ECM is that it cannot capture battery's internal operating states at half-cell level, which are essential in maximizing cell performance without sacrificing lifetime and causing safety issues. For example, when the local anode potential drops below 0 V vs Li/Li^+, lithium plating occurs [11–13] which reduces the battery's available energy capacity due to loss of lithium inventory. The formation of dendrites from plated lithium can lead to internal short-circuits [14–16]. The mainstream LIBs with graphite negative electrode (NE) are particularly vulnerable to lithium plating due to the low NE potential, especially under fast charging conditions.

Real-time monitoring of the NE potential is a significant step towards preventing lithium plating and prolonging battery life. A quasi-reference electrode (RE) can be embedded inside the battery to directly measure the NE potential, which enables a quantitative evaluation of various electrochemical aspects of the battery's internal electrochemical reactions, such as the distinct contribution of each electrode to the overall battery performance [17]. Several studies [18–20] have demonstrated the use of a RE to aid the design of fast charging profiles that do not

Abbreviations: BMS, battery management system; CC, constant current; CV, constant voltage; ECM, equivalent circuit model; EKF, extended Kalman filter; LIB, lithium-ion battery; NE, negative electrode; OCV, open circuit voltage; PE, positive electrode; RC, resistor-capacitor pair; RMSE, root mean square error; SoC, state of charge.

* Corresponding author.
E-mail address: cheng.zhang@coventry.ac.uk (C. Zhang).

https://doi.org/10.1016/j.est.2022.104362
Received 23 November 2021; Received in revised form 18 January 2022; Accepted 2 March 2022
Available online 16 March 2022

violate the NE potential threshold. For example, Liu et al. [18] developed a lithium-plating-free fast charging profile using a RE to prevent the NE potential from dropping below 10 mV vs Li/Li^+. The long-life stability and low polarisation of the chosen RE in the battery's internal environment was verified experimentally. Compared with the manufacturer's fast charging strategy, the proposed strategy achieved twice the charging speed with similar ageing impact on the battery cell within the first 100 charging cycles. One limitation of these studies is that the charging current is controlled in steps starting from the highest allowable value [18–20], and when the NE potential threshold is reached, the current steps down. Using this greedy algorithm for current control cannot guarantee to find the optimal charging profile. A battery model is essential to achieve the optimal stepless charging profile, e.g., to minimise the charging time using optimal control algorithms. Further, while the use of RE in LIBs is essential for validation in offline studies in the laboratory environment, its deployment in a commercial battery pack in electric vehicles is challenging for both cost and safety reasons associated with the risk of short circuits and the combustible nature of the electrolyte [17].

Because embedding sensors inside the battery is generally difficult, a more desirable solution is to estimate the NE potential using virtual-sensor or model-based estimation algorithms. The dynamics of the battery's per-electrode potential can be described by an electrochemical model, such as the pseudo-2D or single particle model [21,22], which enable the application of a state observer or a controller for real-time estimation and control of the physical states inside the battery [23]. However, the computational complexity of these physics-driven models is very high, making it unsuitable for onboard implementation in a commercial BMS with limited computing and storage capacity. Although a reduced order model can be developed [5,22,24], the full-order physical models still need to be parametrised before the model order reduction procedure can be implemented. However, the parametrisation of those physics-informed battery models are very complex and challenging [25,26].

Apart from physical models, data-driven methods have also been developed for real-time estimation of the NE potential. Lin et al. [27] proposed a long short term memory neural network that predicts the anode potential by using the onboard measurable signals including the battery's terminal current, voltage, state of charge, and surface temperature. The model was trained using simulation data generated from an experimentally validated pseudo-2D model supplemented by a two-state thermal model. In another study, Hamar et al. [28] compared three NE potential estimation methods in terms of their accuracy and storage requirements. The test data for model training were generated using a Pseudo-2D model. The advantage of the data-driven model is that it does not involve a deep understanding of the electrochemistry or tedious parameter tuning [27,28]. However, a large amount of data is generally required for model training to ensure effectiveness. For example, a national high performance computing cluster was used to train the neural networks model in [27]. Another limitation of these studies [27,28] is that the NE potential estimation is not validated using experimental data.

Zhao et al. [29] developed a half-cell ECM for capturing the dynamics of the per-electrode potential of LIBs. The model was parametrised using simulation data from a pseudo-2D model and showed high accuracy in predicting the battery's NE potential under multi-rate constant current charging simulation. However, the model is not validated with experimental data of NE potential measurements. Drees et al. [30] developed a fast charging method to reduce the process cost of cell formation based on an half-cell level ECM, and the model is parametrised using special 3-electrode test cells (PAT-Cells from EL-Cell GmbH). However, these studies [29,30] did not address the problem of real-time tracking of NE potential with initial estimation error.

The contribution of this paper is summarised as follows. An easy-to-implement ECM is developed for capturing the dynamics of the battery's per-electrode potential. The developed model is validated with experimental test data from a commercial 21700 cylindrical LIB cell with a reference electrode embedded for separate anode and cathode potential measurements. A novel parameterisation method is developed to optimise the ECM parameters. Finally, based on the developed model, an extended Kalman filter (EKF) is implemented to enable real-time estimation of the NE potential and SoC from cell-level measurements. Experimental results show that both the half-cell model and the EKF estimator achieve high accuracy. The developed algorithm is expected to be suitable for implementation in commercial BMS due to the low computational complexity.

2. Battery and test data

2.1. Test setup

The battery selected in this paper is a 5 Ah, cylindrical LIB cell (LG INR21700-M50). A Biologic VMP3 multi-channel potentiostat is used for charging/discharging the cell placed inside a thermal chamber (Binder MK720) that maintains the ambient temperature at constant 25 °C. The operating range of the battery test channel of VMP3 is ±5A and 0–5 V. The current and voltage measurement accuracy is within 0.1% FSR (full scale range). A K-type thermocouple is attached to the cell at middle-height to monitor the battery's temperature response using a PicoLog data logger. The temperature measurement accuracy is around ±0.5 °C for the K-type thermocouples used in this study.

2.2. RE preparation and implementation

Lithium metal reference electrodes embedded in a cell monitor the anode and cathode electrochemical potentials during battery testing. Standard reference electrodes, such as Standard Hydrogen Electrode (SHE) are impossible to fit inside a commercial Li-ion cell format (due to geometrical constraints and chemical incompatibility), thus alternatives such as pure metals are used instead [19,31]. Unlike a standard reference electrode, the lithium metal quasi-reference electrode does not exhibit a controlled concentration of common ion in the adjacent phases. The RE technology used in this paper has been experimentally validated in previous studies for cell monitoring and developing fast charging profiles [19,31,32]. Fig. 1 shows an assembled lithium reference electrode.

For this study, 7 mm lithium foil was used. A nickel-coated copper wire current collector was attached to the open end of the lithium strip. The assembly was covered with polyimide tape to prevent shorting with the cell positive cap, with the exception of the sensing section to allow ionic contact with the jellyroll. The reference electrode was inserted into the cell utilising the empty space on top of the jellyroll, subsequently the cathode cap was re-seated and the cell can re-sealed with a resin. All of the above operations were performed in an argon filled glovebox with

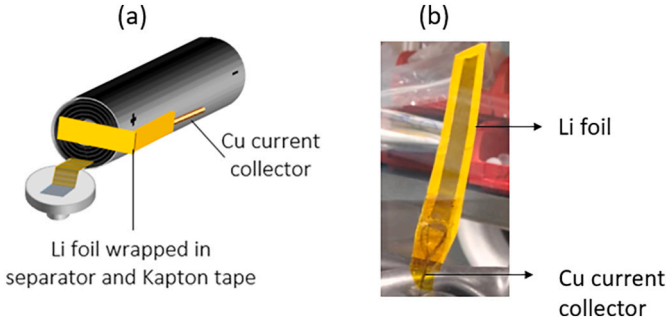

Fig. 1. (a): Schematic diagram of the instrumented cell with reference electrode (RE). (b): A photo of the actual RE. Lithium strip with a copper wire current collector, covered with protective layer of polyimide to prevent shorting with the cylindrical cell cap. This RE assembly was inserted on top of the electrode jellyroll.

O_2 and H_2O levels below 1 ppm. The cells were then transferred into a climate chamber to undergo testing.

2.3. Battery test procedure

The test procedure is summarised in Table 1. It starts with a conditioning protocol using three 0.3C charge-discharge cycles, followed by OCV characterisation at 0.04C, and ends with four pulse charge cycles at different current rates from 0.32C to 0.88C. Here, the battery's nominal capacity is 5 Ah, such that 1C = 5A. The tests were all conducted at 25 °C ambient temperature. The configuration for each test step is detailed below.

The electrical behaviour of the instrumented cell is tested against two unmodified fresh cells. Under the 0.3C conditioning test and the four pulse current charge tests, between the instrumented cell and the fresh cells, the relative difference of the battery capacity is within 0.03%; and the relative difference of the voltage response is within 0.3% at the medium-to-high SoC range where the developed model is validated. The comparison results confirm that the effect of the embedded RE on the cell's capacity and terminal voltage response is negligible. The details of cell comparison can be found in the Supplementary Material.

2.3.1. Cell conditioning tests at 0.3C

The charge step uses a standard constant current constant voltage (CCCV) profile. The CC stage current is 0.3C. The CV stage voltage is 4.2 V with a cut-off current at 0.01C. The discharge step uses a CC discharge at 0.3C till the cut-off voltage at 2.5 V.

2.3.2. OCV characterisation tests at 0.04C

After the conditioning test, the cell is fully charged using the CCCV procedure. The CC stage current is 0.04C and the CV stage voltage is 4.2 V with a cut-off current at 0.01C. The battery's SoC at the end of this CCCV test is set to 100%. Next is a CC discharge at 0.04C till the cut-off voltage at 2.5 V. The test data is shown in Fig. 2.

The potentials of each electrode under this 0.04C charge and discharge cycle are taken as the charging and discharging open circuit voltage (OCV), respectively, and the average value is taken as the mean OCV.

2.3.3. Pulse charging tests at different current rates

In this test step, the battery is always discharged at 0.5C CC until it reaches the cut-off voltage of 2.5 V. Four tests are conducted at different charge current rates, as it is shown in Fig. 3(a). The charging current is a square wave superimposed on a CC. The average currents of the four charging tests in Fig. 3(a) are in sequence [1.6A, 2.5A, 3.8A, 4.4A], or [0.32C, 0.5C, 0.76C, 0.88C]. The square wave has a period of 20s, a duty of 50%, and a magnitude of 0.4A. The superimposed square wave is used to characterise the battery's fast and short-term potential dynamics, while the average CC is used to characterise the slow and long-term dynamics. Fig. 3(c) shows that the maximum observed temperature rise on the battery's surface is 7 °C.

Table 1
Test procedure for the instrumented cell.

Test step	Settings	Limits	Repeat
1, CCCV charge	I = 0.3C	V > 4.2 V, I < 0.01C	3 times
2, CC discharge	I = 0.3C	V < 2.5 V	
3, CCCV charge	I = 0.04C	V > 4.2 V, I < 0.01C	1 time
4, CC discharge	I = 0.04C	V < 2.5 V	
5, Pulse current charge	Average current = 0.32C	V > 4.2 V, I < 0.3C	1 time
6, Pulse current charge	Average current = 0.5C	V > 4.2 V, I < 0.3C	
7, Pulse current charge	Average current = 0.76C	V > 4.2 V, I < 0.3C	
8, Pulse current charge	Average current = 0.88C	V > 4.2 V, I < 0.3C	

3. Data analysis and model development

3.1. Half-cell model structure

The ECM model with separated anode and cathode potential is schematically shown in Fig. 4. The cell-level ECM is divided into the NE and PE sub-models, and each sub-model has a set of OCV element, resistors and capacitors for capturing the half-cell voltage dynamics. According to Kirchhoff's voltage law, the per-electrode potentials are given as follows,

$$\begin{aligned} v_{pe} &= v_{pt} - v_{re} = OCV_{pe} + R_{0,pe} i + v_{1,pe} \\ v_{ne} &= v_{nt} - v_{re} = OCV_{ne} - R_{0,ne} i - v_{1,ne} \end{aligned} \tag{1}$$

where v_{pt}, v_{nt}, v_{re} stand for the potentials of the positive terminal, negative terminal and the reference electrode. i stands for the terminal current and is positive for charging and negative for discharging. $v_{1,\,pe}$, $v_{1,\,ne}$ stand for the over-potentials of the RC networks in the sub-model of the positive electrode (PE) and NE, respectively. The number of the RC pairs for each electrode sub-model is configurable in the modelling fitting procedure for trade-off between complexity and accuracy [33].

As the dynamics of the PE and NE sub-models mirror each other, for simplicity, in the following text only the description of the PE sub-model is presented.

The dynamic equations of the PE sub-model are

$$\begin{aligned} SoC(t+dt) &= SoC(t) + \frac{dt}{3600 C_n} i(t) \\ v_{1,pe}(t+dt) &= a_{1,pe} v_{1,pe}(t) + R_{1,pe}\left[1 - a_{1,pe}\right] i(t) \\ v_{pe}(t) &= OCV_{pe}(SoC(t)) + R_{0,pe} i(t) + v_{1,pe}(t) \\ a_{1,pe} &= exp\left(-\frac{dt}{\tau_{1,pe}}\right) \end{aligned} \tag{2}$$

where t stands for time, dt is the sampling period, C_n the nominal capacity of the battery in Ampere-hour, and $\tau_{1,\,pe}$ the time constant of the RC pair. When more than one RC pair is used, their dynamics equations can be added accordingly in the same term as $R_{1,\,pe}C_{1,\,pe}$.

3.2. Parameter dependency on current rate and SoC

It is well established that the battery's internal impedance depends on the SoC and current rate. The dependency of the ECM's resistor values on SoC is generally captured using look up tables [33,34]. Although an extra dimension of the look up tables can be used to capture the parameter dependency on current rate, this formulation is cumbersome and increases the dimension of model parameters, which in turn increases the chance of parameter fluctuations due to over-fitting. This paper develops a new way of describing the current dependency through an careful analysis of the properties of the battery's internal resistance.

With the PE OCV characterised from the 0.04C test and the PE potential v_{pe} directly measurable using the RE, the total over-potential across the resistors of the PE sub-model can be expressed as follows,

$$v_{op,pe} = v_{pe} - OCV_{pe} = R_{0,pe} i + v_{1,pe} \tag{3}$$

The average current of the pulse charging test (the square wave current shown in Fig. 3) is denoted by i_{ave}, such that the effective total internal resistance of the PE can be written as,

$$R_{eff,pe} = \frac{v_{op,pe}}{i_{ave}} \tag{4}$$

The dependence of the calculated $R_{eff,\,pe}$ on cell SoC and i_{ave} is shown in Fig. 5. The average current rates i_{ave} are given in the legends in Fig. 5. The fluctuations of the $R_{eff,\,pe}$ shown in the augmented subplot are caused by the square wave charging current. It is clear that current rate has a high impact on the PE's impedance. For example, at around 50% SoC, the $R_{eff,\,pe}$ increases by about 50% when the i_{ave} decreases from 4.4A

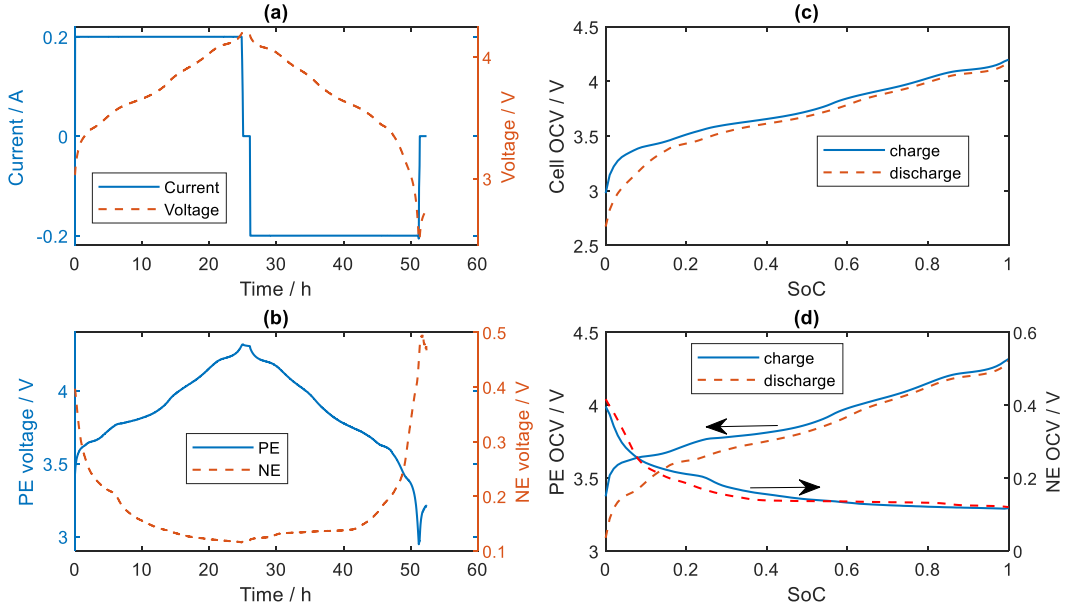

Fig. 2. 0.04C charge and discharge test for OCV characterisation. (a): Terminal current and voltage. (b) PE and NE voltages. (c): Cell OCV under charging and discharging. (d) PE and NE OCV under charging and discharging.

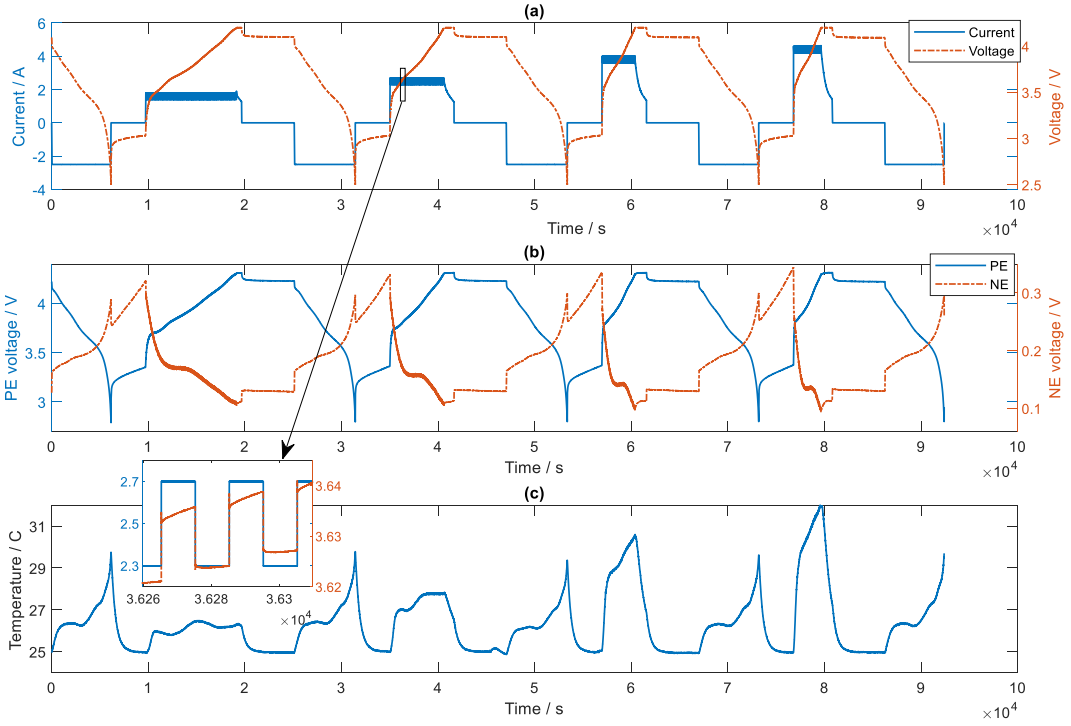

Fig. 3. Battery charging tests at 25 °C ambient temperature. (a): Terminal current and voltage. (b): PE and NE voltage. (c): Battery's surface temperature.

to 1.6A. Further, the dependency of $R_{eff,\ pe}$ on i_{ave} varies noticeably before and after a crossover point located around 27% SOC, which indicates a change in the battery's internal properties. It generally requires two different models or at least two sets of model parameters within an ECM to capture this kind of crossover behaviour. However, the current work will only focus on the medium to high SOC range, i.e., after this crossover SoC point. This choice is based on two considerations. First, it is shown in [35] that, a nonlinear ECM is required to capture the battery's highly nonlinear dynamics in the low SoC range. However, this nonlinear ECM increases the model complexity, and the identification of parameters is also complex. Second, the NE potential drops as the SoC increases. Therefore, in the medium to high SOC range the NE potential is at its lowest, increasing the chance of plating at high SoC, which is the mechanism of interest in this study.

A couple of SoC breakpoints are chosen in Fig. 5 including the inflection points of the $R_{eff,\ pe}$ vs SoC curve. The average $R_{eff,\ pe}$ at these SoC knots are then calculated by smoothing out the fluctuations, and the results are plotted in Fig. 6(a). It shows a nonlinear dependency of $R_{eff,\ pe}$ on current, which increases the complexity of parameter optimisation. Therefore, the parameter dependency on current is linearised using a nonlinear transformation as follows,

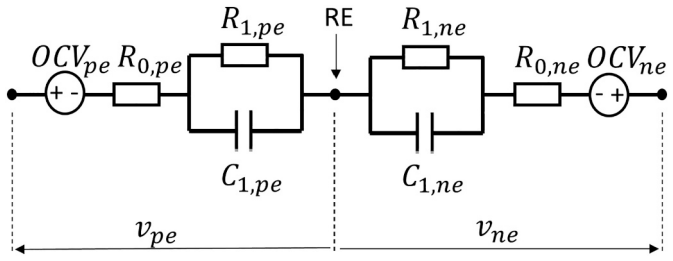

Fig. 4. Schematic representation for ECM with separate potentials for the two electrodes.

$$R_{eff,pe}(i, SoC) = R_{eff,pe,0}(SoC) + R_{eff,pe,1}(SoC)\frac{1}{i^2 + a_{0,pe}} \quad (5)$$

where $a_{0,\,pe}$ is a constant, and $R_{eff,\,pe,\,0}$, $R_{eff,\,pe,\,1}$ are dependent on SoC. The linearisation results are shown in Fig. 6(b). After this transformation, the model parameters $R_{eff,\,pe,\,0}$, $R_{eff,\,pe,\,1}$ become linear-in-the-parameter, which is a desirable property that can significantly improve the parameter optimisation efficiency.

Finally, the series resistor $R_{0,\,pe}$ is characterised using the current jump points in the square wave, i.e.,

$$R_{0,pe} = \frac{v_{pe}(t+dt) - v_{pe}(t)}{i(t+dt) - i(t)}, \text{where } |i(t+dt) - i(t)| = 0.4 \text{ A}$$

and the results are given in Fig. 6(c). It shows that $R_{0,\,pe}$ is dependent on SoC but relatively much less dependent on the current. Therefore, the dependency of $R_{eff,\,pe}$ on current is attributed to the resistor $R_{1,\,pe}$ of the RC network, i.e.,

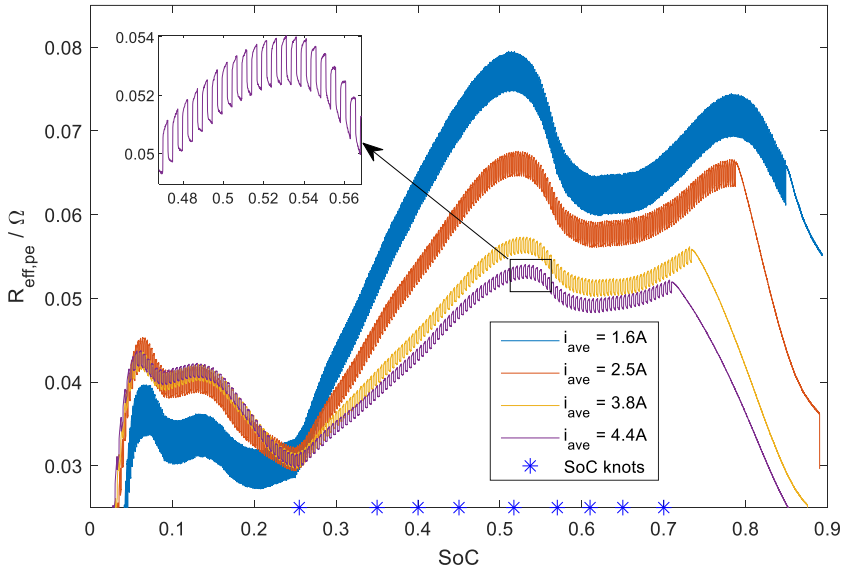

Fig. 5. The dependency of the effective total internal resistance of the PE sub-model on SoC and current rate. $R_{eff,\,pe}$ is calculated using Eq. (4) by processing the pulse charging test data at different current rates.

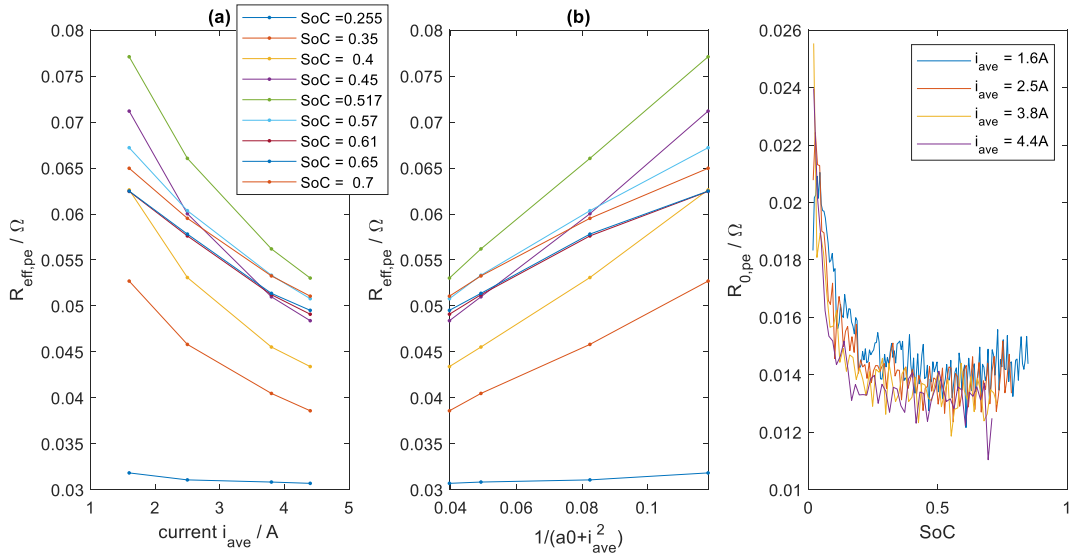

Fig. 6. Analysis of the dependency of the internal resistance of the PE half-cell on current rate. (a): Original data. (b) Linearisation of this current dependency. (c) Characterisation of series resistor $R_{0,\,pe}$.

$$R_{1,pe}(i,SoC) = R_{1,pe,0}(SoC) + R_{1,pe,1}(SoC)\frac{1}{i^2 + a_{0,pe}}$$
$$R_{0,pe} = R_{0,pe}(SoC) \tag{6}$$

The same data analysis procedure is performed for the NE sub-model.

3.3. Model parameter optimisation

The above analysis of the battery's internal resistance is then integrated into the model equations. By substituting Eq. (6) into Eq. (2), we get the following,

$$v_{1,pe}(t+dt) = a_{1,pe}v_{1,pe}(t) + \left[R_{1,pe,0}(SoC) + R_{1,pe,1}(SoC)\frac{1}{i^2 + a_{0,pe}}\right]\left[1 - a_{1,pe}\right]i(t)$$
$$v_{pe}(t) - OCV_{pe}(SoC(t)) = R_{0,pe}(SoC)i(t) + v_{1,pe}(t) \tag{7}$$

The recently developed ECM parametrisation algorithm in [36] is adopted here to optimise the model parameters. One novelty of this optimisation algorithm in [36] is that the time constant is fixed (independent of SoC and current) which significantly reduces optimisation complexity. The SoC-dependent resistor values are optimised all-at-once, and necessary constraints can be incorporated to ensure smooth parameter transition in the full SoC range. The readers are directed to [36] for the parametrisation algorithm details. The parameter optimisation procedure for the PE and NE sub-models is detailed in the Supplementary material.

3.4. Extended Kalman filter to correct initial state estimation error

Due to the difficulty of implementing an RE in a commercial battery pack in real-world operation, the NE potential is not a measurable property from the perspective of the BMS and must be estimated using the developed battery model and the onboard measurements of the battery's terminal current and voltage.

The overall equations of the cell-level model are summarised as follows,

$$SoC(t+dt) = SoC(t) + \frac{dt}{3600C_n}i(t)$$
$$v_{1,pe}(t+dt) = a_{1,pe}v_{1,pe}(t) + \left[R_{1,pe,0}(SoC) + R_{1,pe,1}(SoC)\frac{1}{i^2 + a_{0,pe}}\right]\left[1 - a_{1,pe}\right]i(t)$$
$$v_{1,ne}(t+dt) = a_{1,ne}v_{1,ne}(t) + \left[R_{1,ne,0}(SoC) + R_{1,ne,1}(SoC)\frac{1}{i^2 + a_{0,ne}}\right]\left[1 - a_{1,ne}\right]i(t) \tag{8}$$
$$v(t) = OCV_{pe}(SoC(t)) - OCV_{ne}(SoC(t)) + R_{0,pe}(SoC)i(t) + v_{1,pe}(t) + R_{0,ne}(SoC)i(t) + v_{1,ne}(t)$$

This is a standard nonlinear state-space formulation. Therefore, an EKF can be implemented to correct the initial estimation error of the battery's states and the per-electrode potential. The EKF implementation procedure can be found in textbooks and publications [37,33], and is therefore omitted here.

4. Results and discussion

4.1. Model validation

The validation of the half-cell level ECM with separated electrode potentials was performed using the experimental data of multi-rate pulse current charging tests. Currents of 1.6A, 2.5A, 3.8A and 4.4A were applied in a climate chamber with controlled ambient temperature at 25 °C.

The three data sets (current i = [1.6A, 2.5A, 4.4A]) were used for model training and parameter optimisation, and the data set (i = 3.8A) was used for model validation. It was found that a high model accuracy was already achieved with only 1 RC pair for both the PE and NE sub-models. The time constant of the NE and PE RC pair was the same (fixed at 238 s). It is noteworthy that if more test data are used for model training, such as field drive cycles, more RC pairs might be required to achieve a desired accuracy. The number of the RC pairs, as well as the RC time constants, can be optimised separately for each electrode sub-model using the developed parameter optimisation algorithm in order to achieve high model accuracy under a wider range of operating conditions.

The results of model prediction and experimental measurements are compared in Fig. 7. The star points on the SoC curves in Fig. 7(a,2)–(d,2) indicate the crossover point of 25% SoC, as mentioned above. It is visible that in all four charging cases, the simulated terminal voltage does not match the experimental result when the SoC is lower than the crossover point. This is because the test data in the lower SoC range was not used in model training as mentioned in Section 3.2, such that the developed model focuses on the medium-to-high SoC range. 3.2

For SoC values higher than the crossover point, the model shows high accuracy in capturing both the cell and the NE voltage profiles under all four charging current rates. The root mean square errors (RMSEs) of the cell voltage after the SoC crossover point for the four current rates ([1.6A, 2.5A, 3.8A, 4.4A]) are [1.14 mV, 1.79 mV, 1.97 mV, 1.51 mV] respectively. The RMSEs of the NE voltage for the four current rates are in turn [0.82 mV, 1.25 mV, 0.85 mV, 0.72 mV]. It is worth noting that the developed half-cell model can accurately capture the cell and NE voltage in both the CC and CV charging stages. These results indicate that the parametrised ECM with resolution on anode/cathode is suitable for capturing the electrical behaviour both for the whole cell and the internal NE within the given SoC and current range. The validated model provides the basis for accurate prediction and estimation of the NE potential in real-time.

4.2. State estimation for NE potential and SoC

As an efficient and simple estimation method, EKF is implemented to the established ECM. The accuracy and effectiveness of the ECM combined with EKF is validated in this section. The estimation starts after the crossover point at 25% SoC where the model is valid. The initial SoC guess is deliberately set at 15%, with 10% error. The initial voltages of the RC networks are set to be zero, which also induces initial errors, because an over-potential across the RC pairs would have built-up during charging before the SoC crossover point. The state estimation results under the four charging current rates are shown in Fig. 8. The RMSEs of the NE voltage estimation for the four current rates ([1.6A, 2.5A, 3.8A, 4.4A]) are [2.37 mV, 4.54 mV, 6.70 mV, 7.48 mV] respectively. After the estimation convergence point, the NE voltage error is maintained below 3 mV.

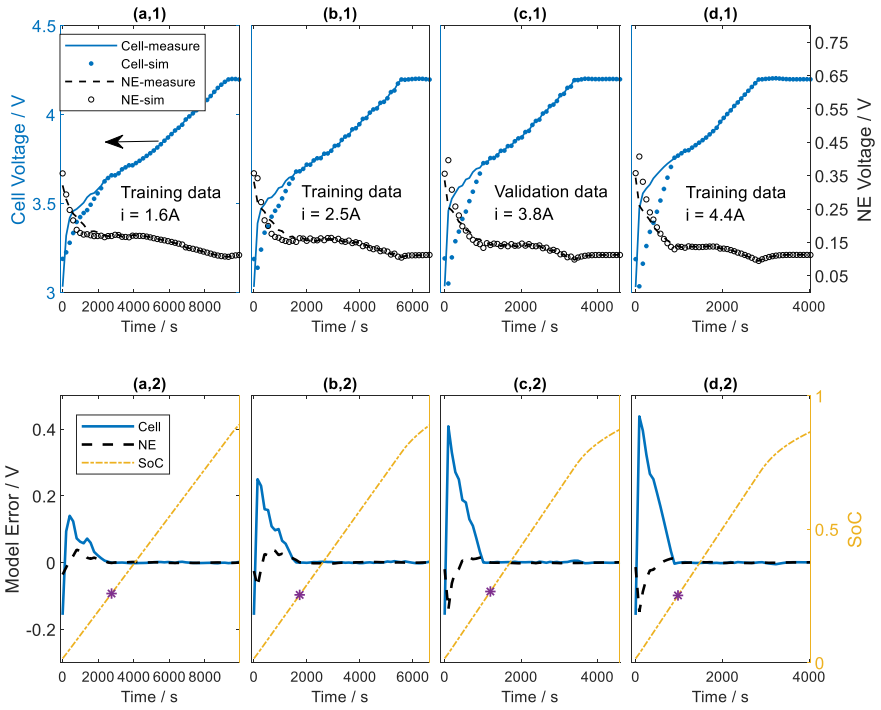

Fig. 7. Modelling results. (a,1) (b,1) (c,1) (d,1) show the fitting results of the cell and NE voltage under the four charging rates [1.6A, 2.5A, 3.8A, 4.4A]. (a,2) (b,2) (c,2) (d,2) show the cell and NE voltage errors as well as the SoC curve. The star points on the SoC curves indicate the crossover point. A high accuracy is achieved in the medium-to-high SoC range (i.e., after the star points) where the model is trained.

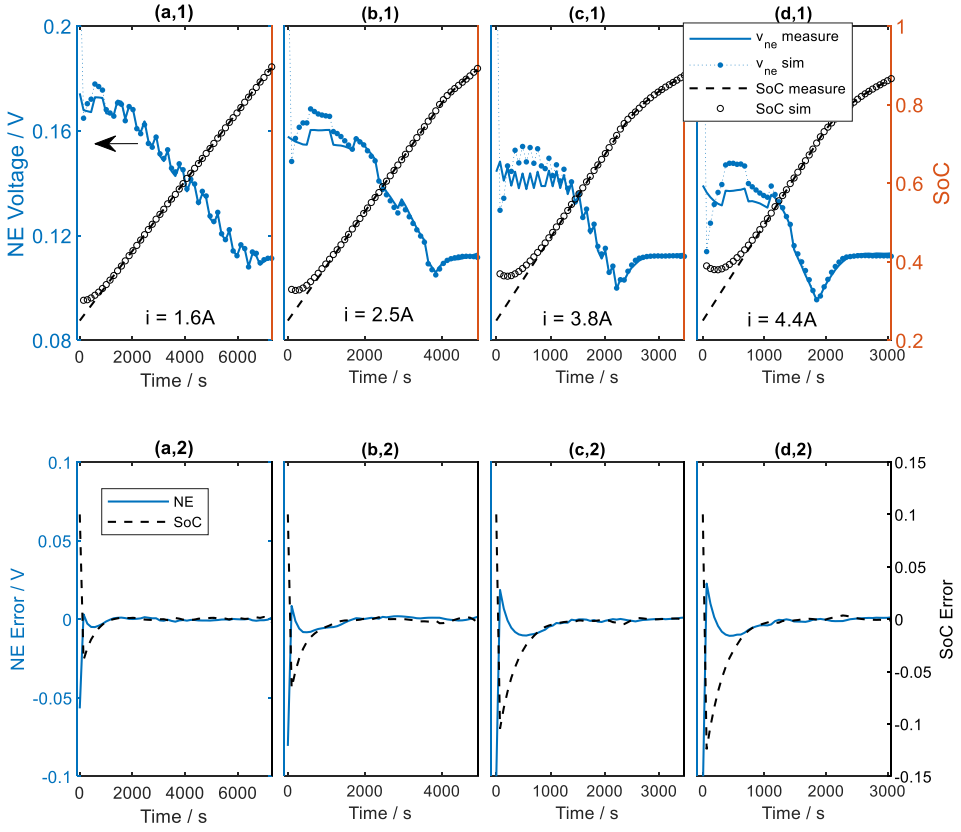

Fig. 8. EKF estimation results. (a,1) (b,1) (c,1) (d,1) show the estimation results of the NE voltage and SoC under the four charging rates [1.6A, 2.5A, 3.8A, 4.4A]. (a,2) (b,2) (c,2) (d,2) show the estimation error of the NE voltage and SoC.

The implementation of EKF on the established ECM not only enables NE potential estimation, but also benefits the accurate estimation of SoC, which is also a key parameter for the cell. The results for SoC estimation are also shown in Fig. 8. It shows that the EKF can effectively correct the initial error in SoC estimation. The RMSEs of the SoC estimation for the four current rates are in turn [0.96%, 1.71%, 2.88%, 3.46%], and after the estimation convergence point the SoC error is maintained below 1%.

Therefore, the accuracy of this framework of half-cell level ECM with EKF is validated for NE voltage and SoC estimations. Because the developed ECM has the advantage of low complexity to facilitate practical implementation in commercial BMS, it provides a viable solution for prolonging lifetime and enhancing battery systems' safety.

5. Conclusion

The widely used full-cell level equivalent circuit model (ECM) of lithium ion battery (LIB) has a significant limitation, as it cannot capture the battery's internal dynamics. To address this issue, a half-cell level ECM is developed in this paper. A cylindrical 21700 LIB cell instrumented with a reference electrode is used to collect experimental test data of the battery's per-electrode potential to enable model parametrisation and validation. A parsimonious and easy-to-implement method is proposed to capture the dependency of model parameters on current rate. Based on the developed new ECM, an extended Kalman filter (EKF) is implemented for real-time estimation of the negative electrode (NE) voltage and state of charge (SoC) using only onboard available singles including the terminal current and voltage. Experimental results confirm that the developed algorithms achieve high modelling and estimation accuracy of the NE potential (RMSE $<$8 mV). The RMSE of SoC estimation is below 3.5%. After the convergence of the EKF, the estimation errors of the NE potential and the SoC are maintained below 3 mV and 1%, respectively.

Real-time estimation of the battery's internal operating conditions, especially the NE potential and SoC, is of high significance to industrial applications, because it can expand the operating envelope of the battery to maximize performance while minimising ageing impact. Real-time NE potential estimation is key to preventing lithium plating for mainstream LIBs with graphite NE. This paper demonstrates that it is feasible to achieve this target using a real-time capable model that is suitable for practical implementation into commercial BMS. Therefore, this work should be of high interest to academic and industry researchers in area of battery energy storage.

There are a few limitations identified in this study. Due to the difficulty of embedding a reference electrode inside the battery in practical applications, the model and estimation algorithms proposed in this paper have to be parametrised offline, which makes it difficult to capture the battery parameters varying over time due to ageing. Further, the battery tests are conducted under only one ambient temperature and the current rate is limited to values below 1C to prevent high temperature rise, therefore the temperature effect is not considered in this work. Since the model parametrisation algorithm used in this paper can apply to a range of current and temperature levels, as it is shown in [36], the framework developed in this paper can be used in future studies e.g., with higher charging current under different temperature levels to capture the coupled electro-thermal properties of LIBs.

CRediT authorship contribution statement

Cheng Zhang: Writing - Original draft, Formal analysis.
Tazdin Amietszajew: Resources, Investigation, Writing - Reviewing and editing.
Shen Li: Conceptualization, Writing - Review & editing.
Greg Offer: Conceptualisation, Writing - Reviewing and editing, Funding acquisition.
Monica Marinescu: Conceptualisation, Writing - Reviewing and editing, Funding acquisition.
Chongming Wang: Writing - Review & editing.
Yue Guo: Supervision.
Rohit Bhagat: Supervision, Writing - Reviewing and editing.

Declaration of competing interest

The authors declare that they have no known competing financial interests or personal relationships that could have appeared to influence the work reported in this paper.

Acknowledgement

The authors would like to acknowledge the support from EPSRC Faraday Institution Multi-Scale Modelling project (EP/S003053/1, grant number FIRG003) and Innovate UK WIZer project (grant number 104427).

Appendix A. Supplementary data

This supplementary material consists of two sections. Section 1 compares the electrical properties of the instrumented cell with a reference electrode and two unmodified fresh cells. The parameter optimisation method of the equivalent circuit model with separate electrode potential is presented in Section 2. Supplementary data to this article can be found online at https://doi.org/10.1016/j.est.2022.104362.

References

[1] IEA, Global EV outlook 2021, Int. Energy Agency, 2021.
[2] L. Lu, X. Han, J. Li, J. Hua, M. Ouyang, A review on the key issues for lithium-ion battery management in electric vehicles, J. Power Sources 226 (2013) 272–288.
[3] C. Zhang, K. Li, S. McLoone, Z. Yang, Battery modelling methods for electric vehicles-a review, in: European Control Conference (ECC), 2014, 2014, pp. 2673–2678.
[4] A. Seaman, et al., A survey of mathematics-based equivalent-circuit and electrochemical battery models for hybrid and electric vehicle simulation, J. Power Sources 256 (2014) 410–423.
[5] L. Li, et al., Lithium-ion battery cathode and anode potential observer based on reduced-order electrochemical single particle model, J. Energy Storage 44 (2021), 103324, https://doi.org/10.1016/j.est.2021.103324.
[6] B. Jiang, H. Dai, X. Wei, L. Zhu, Z. Sun, Online reliable peak charge/discharge power estimation of series-connected lithium-ion battery packs, Energies 10 (3) (2017) 390.
[7] S. Wang, C. Fernandez, C. Yu, Y. Fan, W. Cao, D.-I. Stroe, A novel charged state prediction method of the lithium ion battery packs based on the composite equivalent modeling and improved splice Kalman filtering algorithm, J. Power Sources 471 (2020), 228450.
[8] X. He, B. Sun, W. Zhang, X. Fan, X. Su, H. Ruan, Multi-time scale variable-order equivalent circuit model for virtual battery considering initial polarization condition of lithium-ion battery, Energy 224 (2022), 123084.
[9] K. Liu, K. Li, C. Zhang, Constrained generalized predictive control of battery charging process based on a coupled thermoelectric model, J. Power Sources 347 (2017) 145–158.
[10] K. Liu, K. Li, Z. Yang, C. Zhang, J. Deng, An advanced Lithium-ion battery optimal charging strategy based on a coupled thermoelectric model, Electrochim. Acta 225 (2017) 330–344.
[11] P. Arora, M. Doyle, R.E. White, Mathematical modeling of the lithium deposition overcharge reaction in lithium-ion batteries using carbon-based negative electrodes, J. Electrochem. Soc. 146 (10) (1999) 3543–3553, https://doi.org/10.1149/1.1392512.
[12] S. Schindler, M. Bauer, M. Petzl, M.A. Danzer, Voltage relaxation and impedance spectroscopy as in-operando methods for the detection of lithium plating on graphitic anodes in commercial lithium-ion cells, J. Power Sources 304 (2016) 170–180, https://doi.org/10.1016/j.jpowsour.2015.11.044.
[13] M. Tang, P. Albertus, J. Newman, Two-dimensional modeling of lithium deposition during cell charging, J. Electrochem. Soc. 156 (5) (2009) A390, https://doi.org/10.1149/1.3095513.
[14] T. Waldmann, M. Kasper, M. Wohlfahrt-Mehrens, Optimization of charging strategy by prevention of lithium deposition on anodes in high-energy lithium-ion batteries–electrochemical experiments, Electrochim. Acta 178 (2015) 525–532.
[15] D. Ren, et al., Investigation of lithium plating-stripping process in li-ion batteries at low temperature using an electrochemical model, J. Electrochem. Soc. 165 (10) (2018) A2167–A2178, https://doi.org/10.1149/2.0661810jes.
[16] D. Anseán, et al., Operando lithium plating quantification and early detection of a commercial LiFePO4 cell cycled under dynamic driving schedule, J. Power Sources 356 (2017) 36–46, https://doi.org/10.1016/j.jpowsour.2017.04.072.

[17] R. Raccichini, M. Amores, G. Hinds, Critical review of the use of reference electrodes in li-ion batteries: a diagnostic perspective, Batteries 5 (1) (2019) 12.
[18] J. Liu, et al., Lithium-plating-free fast charging of large-format lithium-ion batteries with reference electrodes, Int. J. Energy Res. 45 (5) (Apr. 2021) 7918–7932, https://doi.org/10.1002/er.6375.
[19] T. Amietszajew, E. McTurk, J. Fleming, R. Bhagat, Understanding the limits of rapid charging using instrumented commercial 18650 high-energy li-ion cells, Electrochim. Acta 263 (2018) 346–352, https://doi.org/10.1016/j.electacta.2018.01.076.
[20] S.P. Rangarajan, Y. Barsukov, P.P. Mukherjee, Anode potential controlled charging prevents lithium plating, J. Mater. Chem. A 8 (26) (2020) 13077–13085.
[21] M. Doyle, T.F. Fuller, J. Newman, Modeling of galvanostatic charge and discharge of the lithium/polymer/insertion cell, J. Electrochem. Soc. 140 (6) (1993) 1526–1533, https://doi.org/10.1149/1.2221597.
[22] S.J. Moura, F.B. Argomedo, R. Klein, A. Mirtabatabaei, M. Krstic, Battery state estimation for a single particle model with electrolyte dynamics, IEEE Trans. Control Syst. Technol. 25 (2) (2017) 453–468.
[23] B. Suthar, P.W.C. Northrop, R.D. Braatz, V.R. Subramanian, Optimal charging profiles with minimal intercalation-induced stresses for lithium-ion batteries using reformulated pseudo 2-dimensional models, J. Electrochem. Soc. 161 (11) (2014) F3144–F3155, https://doi.org/10.1149/2.0211411jes.
[24] Y. Li, B. Xiong, D.M. Vilathgamuwa, Z. Wei, C. Xie, C. Zou, Constrained ensemble Kalman filter for distributed electrochemical state estimation of lithium-ion batteries, IEEE Trans. Ind. Inf. 17 (1) (2021) 240–250, https://doi.org/10.1109/TII.2020.2974907.
[25] M. Ecker, T.K.D. Tran, P. Dechent, S. Käbitz, A. Warnecke, D.U. Sauer, Parameterization of a physico-chemical model of a lithium-ion battery: I. Determination of parameters, J. Electrochem. Soc. 162 (9) (2015) A1836–A1848.
[26] M. Ecker, S. Käbitz, I. Laresgoiti, D.U. Sauer, Parameterization of a physico-chemical model of a lithium-ion battery: II. Model Validation, J. Electrochem. Soc. 162 (9) (2015) A1849–A1857, https://doi.org/10.1149/2.0541509jes.
[27] X. Lin, Real-time prediction of anode potential in li-ion batteries using long short-term neural networks for lithium plating prevention, J. Electrochem. Soc. 166 (10) (2019) A1893–A1904, https://doi.org/10.1149/2.0621910jes.
[28] J.C. Hamar, S.V. Erhard, C. Zoerr, A. Jossen, Anode potential estimation in lithium-ion batteries using data-driven models for online applications, J. Electrochem. Soc. 168 (3) (2021) 30535, https://doi.org/10.1149/1945-7111/abe721.
[29] T. Zhao, Y. Zheng, J. Liu, X. Zhou, Z. Chu, X. Han, A study on half-cell equivalent circuit model of lithium-ion battery based on reference electrode, Int. J. Energy Res. 45 (3) (Mar. 2021) 4155–4169, https://doi.org/10.1002/er.6081.
[30] R. Drees, F. Lienesch, M. Kurrat, Fast charging lithium-ion battery formation based on simulations with an electrode equivalent circuit model, J. Energy Storage 36 (2021), 102345, https://doi.org/10.1016/j.est.2021.102345.
[31] T. Amietszajew, et al., Hybrid thermo-electrochemical in situ instrumentation for lithium-ion energy storage, Batteries Supercaps 2 (11) (2019) 934–940.
[32] T. Amietszajew, J. Fleming, R. Bhagat, Hybrid instrumentation for multi-functional thermodynamic cell monitoring, in: 237th ECS Meeting With the 18th International Meeting on Chemical Sensors (IMCS 2020)(May 10-14, 2020), 2020.
[33] C. Zhang, K. Li, L. Pei, C. Zhu, An integrated approach for real-time model-based state-of-charge estimation of lithium-ion batteries, J. Power Sources 283 (2015) 24–36.
[34] C. Zhang, K. Li, J. Deng, S. Song, Improved realtime state-of-charge estimation of LiFePO4 battery based on a novel thermoelectric model, IEEE Trans. Ind. Electron. 64 (1) (2017) 654–663.
[35] M. Ouyang, G. Liu, L. Lu, J. Li, X. Han, Enhancing the estimation accuracy in low state-of-charge area: a novel onboard battery model through surface state of charge determination, J. Power Sources 270 (2014) 221–237.
[36] X. Hua, C. Zhang, G. Offer, Finding a better fit for lithium ion batteries: a simple, novel, load dependent, modified equivalent circuit model and parameterization method, J. Power Sources 484 (2021), 229117, https://doi.org/10.1016/j.jpowsour.2020.229117.
[37] R.E. Kalman, A new approach to linear filtering and prediction problems, ASME. J. Basic Eng. 82 (1) (1960) 35–45. March.